Using Electrical Resistance Tomography Images to Analyze the Batch and Continuous-Flow Mixing of Pseudoplastic Fluids Possessing Yield Stress in the Agitated Tanks

Dineshkumar Patel, Farhad Ein-Mozaffari*, Mehrab Mehrvar

Department of Chemical Engineering, Ryerson University, Toronto, Ontario, M5B 2K3, Canada
*corresponding author: fmozaffa@ryerson.ca

Abstract Non-ideal flows, such as dead zones and channeling, are commonly occurred in the mixing of non-Newtonian fluids possessing yield stress. It is a challenging task to visualize such phenomena occurring inside the mixing vessels due to the opacity of the fluids. Numerous conventional techniques have been used to study the mixing operations in both batch and continuous modes; however, these techniques have their own limitations as they are not suitable for opaque fluids or they might interfere with the local flow pattern. Therefore, the core objective of this study was to employ electrical resistance tomography (ERT), which is an efficient and non-intrusive flow visualization technique for both opaque and transparent fluids, to study the batch and continuous-flow mixing of non-Newtonian fluids possessing yield stress in a stirred vessel. In this study the ERT technique was employed to: (i) measure the mixing time in the batch mode, (ii) measure the cavern size in the batch mode, (iii) analyze the cavern deformation in the continuous mode, and (iv) visualize the flow pattern generated by the impeller inside the stirred tank in the continuous mode. The 2D and 3D tomography images were used to identify the existence of the non-ideal flows encountered inside the mixing vessel. The ERT data were also used to validate the CFD model. Applying the outcomes of this research can enhance the design criteria of the mixing of non-Newtonian fluids in both batch and continuous modes.
Keywords: Mixing, Non-Newtonian fluids, Tomography, Mixing time, Cavern, Flow Visualization, yield stress, ERT

1 Introduction

Mixing operations are commonly used in the chemical and allied process industries to improve the degree of homogeneity [1]. Mixing of non-Newtonian fluids especially pseudoplastic fluids possessing yield stress plays a major role in pulp and paper, biopolymer, food, biochemical, polymer, pharmaceutical, and cosmetic industries. Mixing of the non-Newtonian fluids exhibiting yield stress results in the formation of the stagnant zones in the stirred vessel away from the impeller, where the impeller-imparted shear stress fails to exceed the fluid yield stress. Moreover, the vast majority of the non-Newtonian fluids are naturally opaque; therefore, it is very challenging to see what is happening inside the mixing vessel. Thus, the design of the mixing systems for the non-Newtonian fluids is more challenging than that for the Newtonian fluids. To evaluate the mixing effectiveness and to characterize the mixing system, the power consumption, mixing time, cavern size, deformation of the cavern, and flow pattern should be determined.

The mixing time offers a powerful approach for the evaluation of mixing effectiveness in the batch mode [2]. Numerous experimental techniques have been employed to measure the mixing time such as thermocouple based techniques [3], conductivity probe [4], colorimetric method [5], dye addition [6], liquid-crystal thermography [7], laser-induced fluorescence [8], and radioactive liquid tracer [9]. Each of these techniques has its own shortcomings. Rielly and Britter [10] observed that mixing time depends on the size of the conductivity probe, thus making the measurement imprecise. The probe also disturbs the flow pattern inside a vessel. Moreover, some of these techniques are not appropriate to opaque fluids, demand transparent vessels, are hazardous to human beings, and are bound to a few monitoring points in the vessel for measuring the mixing time.

To measure the cavern size in the batch mode various experimental techniques such as X-ray photographs [11,12], laser Doppler anemometer [13], planner laser induced [14], coloring with dye [15], hot film anemometer [16], and ultraviolet fluorescence [14] have been employed. Each of these techniques has its own limitations. Hot film anemometer is an invasive method which alters the local flow field. The X-ray technique provides a non-intrusive measurement in opaque fluids. However, the penetration depth of X-ray is restricted by opacity of the fluids used and the vessel wall. Some of these methods (e.g. laser based techniques

and addition of the dye as a tracer) can only be used for transparent fluids while most of the non-Newtonian fluids are opaque.

Some studies have been carried out to investigate the continuous-flow mixing of non-Newtonian fluids in stirred vessels. Using dynamic tests, Ein-Mozaffari et al. [17] and Patel et al. [18] explored the effect of the impeller diameter on the performance of the continuous-flow mixing of non-Newtonian fluids with yield stress. They found that the efficiency of the continuous-flow mixer improved as the impeller diameter was increased. Using ERT and dynamic tests, Patel et al. [19] characterized the continuous-flow mixing of non-Newtonian fluids with yield stress using the ratio of residence time to the batch mixing time. They found that this ratio should be at least 8.2 to achieve ideal mixing; otherwise non-ideal flows are likely to occur in the continuous-flow mixing system. The performance of a continuous-flow mixing system also depends on the fluid rheology [20] and fluid feed flow rate [21,22]. The dynamic test results showed that the extent of non-ideal flows, such as channeling and dead volume, increased when the fluid yield stress as well as the fluid flow rate were increased in the mixing of non-Newtonian fluids exhibiting yield stress [23,24]. Using dynamic tests, Patel et al. [18] also explored the effect of fluid height in the vessel, types of impellers (axial-flow and radial-flow), impeller off-bottom clearance, residence time, and jet velocity on the dynamic performance of the continuous-flow mixing of non-Newtonian fluids. They found that the extent of non-ideal flows decreased when the clearance of the impeller was increased from $H/3.4$ to $H/2.1$ (where H is the fluid height in the vessel) and the jet velocity was increased from 0.317 to 1.66 m s^{-1}. Furthermore, as the fluid height in the vessel was increased, the extent of non-ideal flows also increased. In addition, increasing the residence time of the fluid in the vessel decreased non-ideal flows. Using CFD, Ford et al. [25] studied the fluid flow of pulp suspensions (a non-Newtonian fluid) in an agitated pulp stock chest equipped with a side-entering impeller. They found that with the inlet at the top of the vessel, the extent of non-ideal flows was reduced using the bottom outlet compared to the side outlet. Most of the previous studies have identified non-ideal flows using dynamic tests and CFD in which the data were generally fitted with the dynamic model. Using CFD [26,27], residence time distribution (RTD) [28], laser Doppler velocimetry (LDV) [29] and spectrophotometer [30], some studies have also been carried out in the continuous-flow mixing of Newtonian-fluids in the stirred vessel and found that non-ideal flow such as channeling affect the performance of the mixing system. Newtonian fluids have been commonly used for the study of continuous-flow mixing in stirred tank reactors; however, a few studies have been carried out on the pseudoplastic fluids exhibiting yield stress.

Indeed, a thorough literature review reveals that numerous conventional techniques have been employed to study mixing in batch and continuous modes. However, these techniques have their own limitations as they are not suitable for opaque fluids or they might interfere with the local flow pattern. Therefore, this study aims to employ electrical resistance tomography (ERT), an efficient and non-intrusive measurement technique, to study the batch and continuous-flow mixing of non-Newtonian fluids. In this study the ERT technique was employed to: (i) measure the mixing time in the batch mode (ii) measure the cavern size in the batch mode, (iii) analyze the cavern deformation in the continuous mode, and (iv) visualize the flow pattern generated by the impeller inside the stirred tank in the continuous mode.

2 Experimental Setup and Procedure

In this study, a fully baffled transparent flat-bottomed cylindrical tank with a diameter (T) of 0.38 m and a height of 0.60 m was employed to mix the xanthan gum solutions (Fig. (1)). Four equally spaced baffles with a width of $T/10$ were attached to the wall of the mixing tank. As shown in Fig. (2), the radial-flow impellers (RT and Scaba) with a $T/2.1$ diameter and a close clearance impeller (Maxblend) with a $T/1.5$ diameter were utilized to agitate the non-Newtonian fluids. The off-bottom clearance was set at $T/2.4$, $T/2.4$, and $T/76$ for the Scaba, RT, and Maxblend impellers, respectively. The impeller off-bottom clearances were measured from the centre of the agitator for the Scaba and RT impeller and from the bottom of the impeller for the Maxblend impeller. The mixing tank was equipped with a top-entering impeller driven by a 2-hp motor, and the impeller speed was set to the desired revolution per minute (rpm) using a variable frequency drive. The impeller torque and speed were measured using a rotary torque transducer (Staiger Mohilo, Lorch, Germany) and a tachometer, respectively. The fluid height (H) in the tank was 0.41 m providing a total volume around 0.047 m^3. The diameters of the inlet and outlet pipes were 0.025 m. The fluid flow rate (Q) was maintained at $Q = 1.60 \times 10^{-4}$ $m^3 s^{-1}$. The inlet was located at the top ($r = 0.13$ m, $\Phi = 90^o$, and $z = T$) and the outlet was located at the bottom ($r = 0.13$ m, $\Phi = 315^o$, and $z = 0/T$) of the mixing vessel. Fig. (3) shows a snapshot of the ERT tank with an

arrangement of electrodes on the periphery of the tank. Six tomography sensor planes were positioned around the circumference of the mixing tank. The planes were 0.06 m apart from each other with the bottom plane 0.04 m from the bottom of the tank. The planes were numbered from the top (*P*1) to the bottom (*P*6). Each plane had 16 stainless steel electrodes which were located equidistantly on the periphery of the vessel. The height, width, and thickness of the electrodes were 0.02, 0.03, and 0.001 m, respectively. Each electrode was in direct contact with the working fluid in the tank without invading the flow and was connected to the electrical resistance tomography (ERT) system (P2+ v7.0, Industrial Tomography Systems, Manchester, UK). The tomography machine was connected to a computer for the image reconstruction. The excitation frequency and injection current were set at 9600 Hz and 75 mA, respectively. The frame rate for data collection was about 2 s per frame.

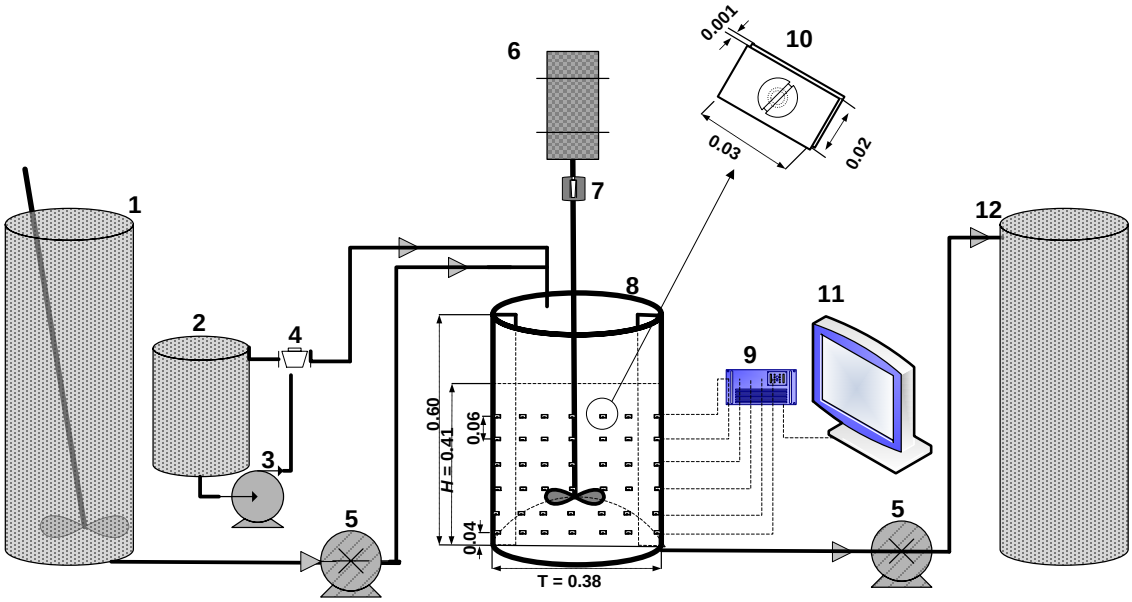

Fig. 1 Experimental set-up (dimensions in m): (1) feed tank, (2) tracer tank, (3) metering pump, (4) solenoid valve, (5) progressive cavity pump, (6) electric motor, (7) torque meter, (8) mixing tank, (9) ERT data acquisition system, (10) electrode, (11) host computer, (12) discharge tank.

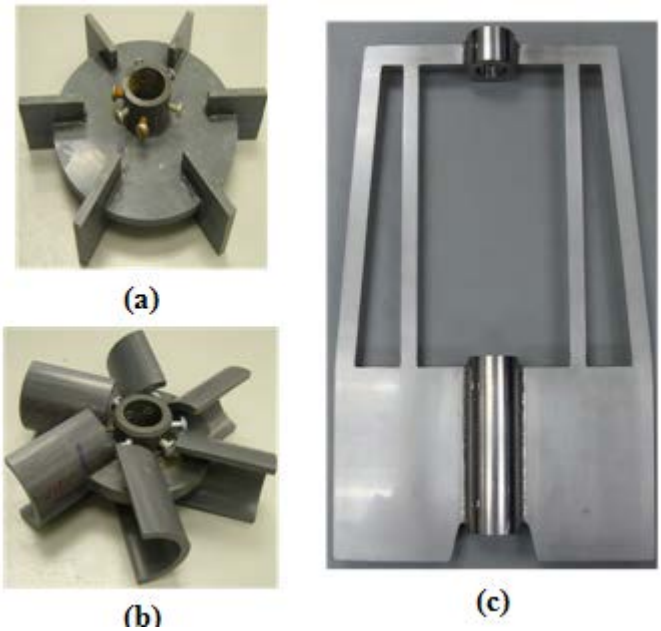

Fig. 2 Impellers employed in this study: (a) RT impeller, (b) 6SRGT Scaba impeller, and (c) Maxblend impeller.

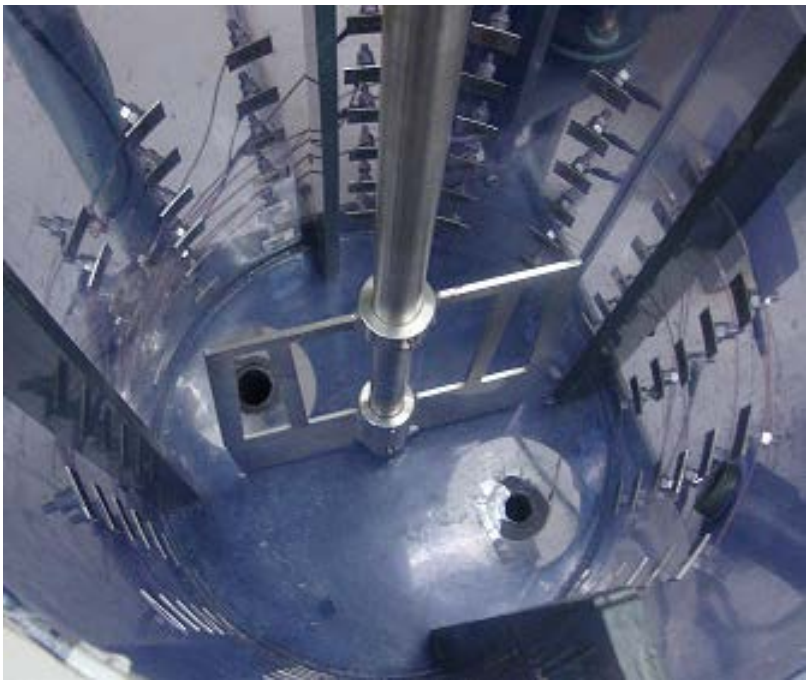

Fig. 3 Tomography electrodes installed on the periphery of the mixing tank.

The mixing time measurement in the batch mode was carried out by injecting 50 mL of 10% saline solution (NaCl) near shaft on plane 1 (r = 0.07 m, Φ = 260°, and z = 0.34 m) using a plastic syringe and monitoring the tracer concentration with time using ERT. To measure the cavern size in the batch mode, 30 mL of 5% saline solution (tracer) was injected near the impeller hub using a plastic syringe and the tracer concentration was monitored using ERT. Measurements were collected from six planes of electrodes until the cavern size remained unchanged. Then tomography images were used to analyze the cavern size. To study the effect of the inlet-outlet flow on the deformation of the cavern, 30 mL of 5% saline solution (tracer) was injected near the impeller hub in the batch mode and the distribution of the tracer concentration was monitored using ERT. Measurements were collected from six planes of electrodes until the cavern size remained unchanged. Once the cavern was fully developed in about 30 s, the feed and discharge pumps were turned on simultaneously and the fluid was pumped from the feed tank to the discharge tank through the mixing vessel. ERT data were collected and the tomography images were reconstructed to visualize the deformation of the cavern inside the mixing vessel. To visualize the flow pattern generated in the continuous-flow mixing, the feed and discharge pumps were turned on simultaneously and fresh fluid was pumped from the feed tank to the discharge tank through the mixing vessel, which did not contain any pre-injected saline solution. 150 mL of 9% saline solution (tracer) was then injected in the feed. Measurements were collected from six planes of electrodes. ERT data were collected and the tomography images were reconstructed to visualize the distribution of the tracer concentration inside the mixing vessel. In all four procedures, before the injection of the tracer, the reference state was taken to eliminate the effect of the stirrer and other internals within the mixing tank. Moreover, the maximum concentration of the tracer in the solution was always below 0.17%. The previous study showed that the rheological properties of the xanthan gum solution did not change significantly when the tracer (NaCl) concentration in the tank was less than 0.17% [24]. The salt was dissolved in distilled water to prepare saline solution. The conductivities of 5, 9 and 10% saline solutions were measured about 56.95, 93.26, 103.2 mS cm^{-1}. In this study, xanthan gum solutions with 0.5, 1.0, and 1.5% mass concentrations were used in this study. The conductivities of 0.5, 1.0, and 1.5% xanthan gum solution were 0.55, 0.98, 1.4 mS cm^{-1}. Xanthan gum solution is a shear-thinning fluid possessing yield stress and its rheological properties can be described by the Herschel-Bulkley model [31] ($\tau_s = \tau_y + K(\dot{\gamma})^n$, where τ_s is the shear stress, τ_y is the yield stress, K is the consistency index, $\dot{\gamma}$ is the shear rate, and n is the power-law index). The rheological properties of the xanthan gum solutions are provided in Table 1 [24]. The experimental conditions for batch and continuous modes are summarized in Table 2.

Table 1. Rheological properties of xanthan gum solutions [24].

Concentration (%)	Density, ρ (Kgm^{-3})	Yield Stress, τ_y (Pa)	Consistency Index, K ($Pa.s^n$)	Power law Index, n
0.5	997.36	1.79	3	0.11
1.0	991.80	5.25	8	0.12
1.5	989.76	7.46	14	0.14

Table 2. Experimental conditions.

Descriptions	Range and types
Impeller types	Close clearance impeller: Maxblend Radial-flow impeller: RT and Scaba
Impeller speed (*N*)	24–160 rpm
Fluid rheology	0.5 and 1.0% xanthan gum solution
Fluid flow rate (*Q*)	$1.60 \times 10^{-4}\ m^3\ s^{-1}$
Inlet locations	*TI* (r = 0.13 m, $\Phi = 90^o$, and z = 0.38 m)
Outlet locations	*BO* (r = 0.13 m, $\Phi = 315^o$, and z = 0.00 m)

2.1 Electrical Resistance Tomography

In this study, the ERT technique was employed to measure the mixing time and cavern size in the batch mode, to analyze the deformation of the cavern due to the inlet-outlet flow, and to visualize the flow pattern in the continuous-flow mixing system. ERT is an efficient method due to its high-speed capability, inherent simplicity, and rugged construction of the tomographer. Therefore, ERT is widely used in various chemical engineering processes such as, to name a few, solid-liquid filtration [32], solid-liquid mixing [33-35], non-Newtonian fluid mixing [19,36,37], airlift bioreactor [38,39], and photoreactor [40].

The aim of the ERT system is to obtain the electrical resistance distribution in the area of interest and it can be acquired by applying currents (or voltages) and measuring voltages (or currents) via electrodes mounted on the boundary of the domain. The sensing, data acquisition, and image reconstruction are the principal elements of the ERT system. The design of electrodes is important to maximize its efficiency to sense conductivity in the area of interest [41]. Electrodes are generally fabricated from platinum, gold, silver, brass, stainless steel or silver palladium alloy [42]. The position of electrode [43], size of electrode [44], and number of electrodes [45] are the key facets in the tomography method. The electrodes, which are located around the boundary of the vessel, make electrical contact with the fluid inside the vessels and are connected to the data acquisition system (DAS) using the co-axial cables to reduce the electromagnetic noise and interference [43].

The data acquisition system (DAS) performs the different task such as signal measurement, de-modulation, filtering, and control; waveform generation and synchronization, multiplexer control (share the current source and voltage measurement stages between any numbers of electrodes), and power supply [46]. Thus, it provides the quantitative data for measuring the conductivity distribution inside the vessel. A misleading image can be rebuilt when the full set of independent measurement is not collected [43]; therefore, it is imperative that the data collection strategy have very good ability to distinguish between two conductivities [47]. An adjacent strategy, opposite strategy, diagonal or cross strategy, and conducting boundary strategy are the main strategies for voltage measurement. Among these, adjacent strategy, which

demands less hardware and provides fast image reconstruction, was used in this study. In the adjacent strategy, the current is applied through two adjacent pair of electrodes and the voltages are measured at the remaining adjacent pair of electrodes. The injection pair is then switched to the next pair of electrodes and repeated until all independent combinations have been completed. This strategy provides 104 individual voltage measurements for a plane with 16 electrodes according to the equation n_e (n_e-3)/2 where n_e is the number of electrodes per plane. Finally, DAS communicates these quantitative data to the host image reconstruction computer, where the data are processed using a suitable image reconstruction algorithm. Generally, two types of algorithm are used to process data for image reconstruction depending on accuracy of image and time required for reconstruction: (1) non-iterative such as the linear back projection algorithm [48] and (2) iterative such as the sensitivity conjugate gradient [49]. A 2D linear back projection (non-iterative) algorithm was employed in this study because the iterative algorithm is often computationally more time consuming and too slow for the real-time image reconstruction compared to the non-iterative algorithm. To map the conductivity distribution, the area of the interest is usually gridded spatially to equal squares. Each individual tomogram consists of a 20 × 20 pixel array giving 400 spatial elements. However, some of these pixels lie outside the vessel circumference and the image is formed from pixels inside the vessel. The circular image is constructed using 316 pixels from 400 pixels square grid. In order to construct the image, linear back projection method [48] was used to compute the value (resistivity distribution) of each pixel in the image from the voltage measurements using $X^{-1}R = V$, where R is a vector describing resistivity distribution, V is a vector describing the surface voltage distribution and X^{-1} is the inverse of the matrix X. Matrix X can be assembled from the sensitivity coefficient (C) at a point (x,y) for a current-driven electrode pair m and voltage measurement electrode pair n [50]:

$$C_{m,n,x,y} = \frac{\Delta V(m,n)}{\Delta R(x,y)} = \int \nabla \phi_m . \nabla \phi_n dA \tag{1}$$

where ϕ_m and ϕ_n are the electric fields generated by each electrode pair m and n and calculated from voltage measurement V. A is the region of interest. The grey-scale value of each pixel, G (x,y), is given by the following equation, which will generate the output image applying the back projection algorithm:

$$G(x,y) = \frac{\sum_{m=1}^{M}\sum_{n=1}^{N} C_{m,n,x,y}\left(\frac{\Delta V}{V}\right)_{m,n}}{\sum_{m=1}^{M}\sum_{n=1}^{N} C_{m,n,x,y}} \tag{2}$$

3 Results and Discussion

3.1 Power

The evaluation of the mixing performances of the impellers is essentially depends on the power consumption. The power (P) consumed by the impellers was calculated using $P = 2\pi NM$, where N and M were the impeller rotational speed and the torque, respectively. The friction torque was subtracted from the torque measured for the impeller rotating in the mixing vessel with fluid. The power number (P_o) was then calculated using $P_o = P/\rho D^5 N^3$, where D and ρ were impeller diameter and the fluid density, respectively. The average shear rate ($\dot{\gamma}_{avg}$) obtained from the Metzner and Otto's correlation [51] ($\dot{\gamma}_{avg} = k_S N$, where k_S is a function of the type of the impeller) was used to estimate the apparent viscosity (η) of the Herschel-Bulkley fluid. The modified Reynolds number (Re) for this type of fluid was calculated as follows:

$$\mathrm{Re} = \frac{\rho N D^2}{\eta} = \frac{k_S \rho N^2 D^2}{\tau_y + K(k_S N)^n} \tag{3}$$

The value of k_S was set at 11.5 [36] and 20 [52] for the radial-flow and the close-clearance impellers, respectively. The power number curves for the RT, Scaba, and Maxblend impellers are depicted in Fig. (4). The trend of the power number curves is similar to that reported in the literature [1]. The results show that at Re < 10 the solid line with a slope of -1 fitted the data precisely for the RT and Scaba impeller, which implies that $P_o Re$ was constant and the flow was in the laminar regime. Further, in the transitional regime, the power

number changed slightly with *Re*. However, in the case of the Maxblend, the laminar region ended at about *Re* = 40. The same value was also reported by Fradette et al. [53] for the Maxblend impeller; however, Iranshahi et al. [54] found a slightly lower value, *Re* = 25, for the Maxblend impeller.

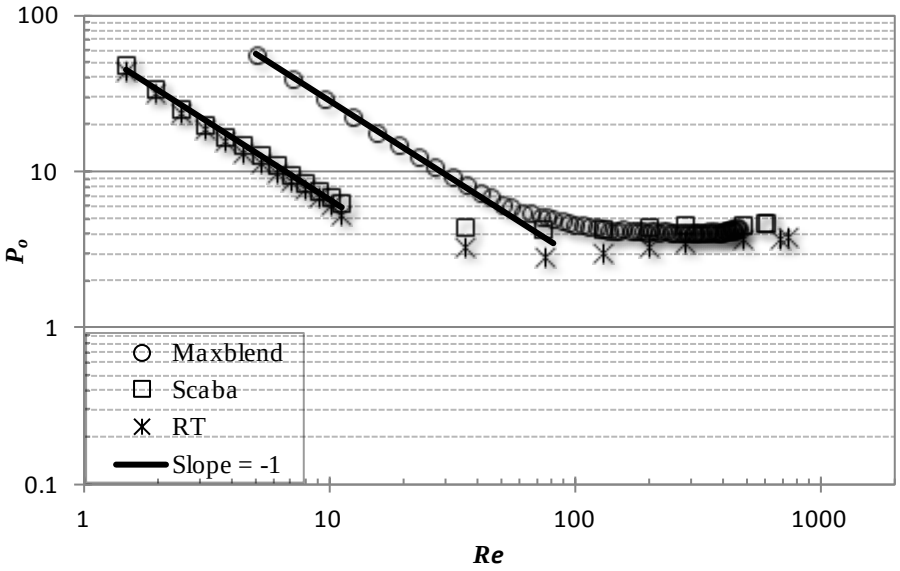

Fig. 4 Power curves for the Maxblend, Scaba, and RT impellers (1.5% xanthan gum).

3.2 Mixing time

The ERT technique was utilized to measure the mixing time. Mixing time is extensively used to evaluate the mixing effectiveness of the system in the batch mode. Mixing time can be defined as the time required achieving a predetermined state of homogeneity by a mixer. In this study, the mixing time (θ) was defined as the time required for the conductivity of the fluid to reach 98% of the steady-state value after the injection of the tracer. As mentioned earlier, 50 mL of the tracer (10% saline solution), which had higher conductivity than the xanthan gum solutions, was injected below the liquid surface on plane 1 at r = 0.07 m, Φ = 260°, and z = 0.34 m. Fig. (5) shows the 2-dimensional (2D) tomograms recorded after the injection of the tracer for the mixing of 1% xanthan gum solution with the Maxblend impeller at N = 160 rpm (*Re* = 474). The red color in these tomograms shows the high-conductivity regions, which represent the higher tracer concentration in those regions. The blue color demonstrates the low-conductivity regions, which indicates the lower tracer concentrations. The blue color in all planes at t = 0 s (before the tracer injection) demonstrates that only xanthan gum solution was present throughout the vessel. At t = 2 s, the color changed from blue to red/green in tomograms, which indicates that the tracer was injected. After 2 s, more amount of the injected salt moved downward and appeared on plane 6. The Maxblend impeller consists of a bottom paddle mounted by the top grids. These grids helped to disperse the tracer at the upper region of the tank. As time proceeded, the tracer was spread in the clockwise direction and dispersed throughout the tank. The time series of 2D tomograms show that a homogenous mixture was obtained after 26 s. The ERT data were also used to plot average conductivity as a function of time for six ERT planes.

Fig. (6) shows a practical approach to measure the mixing time after the injection of the tracer for six tomography planes. It shows that the average conductivity values for all ERT planes reached within 98% of the steady state value after 26 s. The mixing time measurement was conducted when there were no stagnant regions within the tank. This approach was employed to measure the mixing time in this study. Fig. (7) shows the dimensionless mixing time ($N.\theta$) as a function of the Reynolds number (*Re*) for the scaba impeller [36]. The results show that as the impeller rotational speed was increased, the mixing time decreased. As the impeller rotational speed was increased, the shear stress produced by the impeller also increased. At a higher impeller speed the xanthan gum solution was swept away from the impeller, leading to an improved mixing quality by overcoming the yield stress of the fluid.

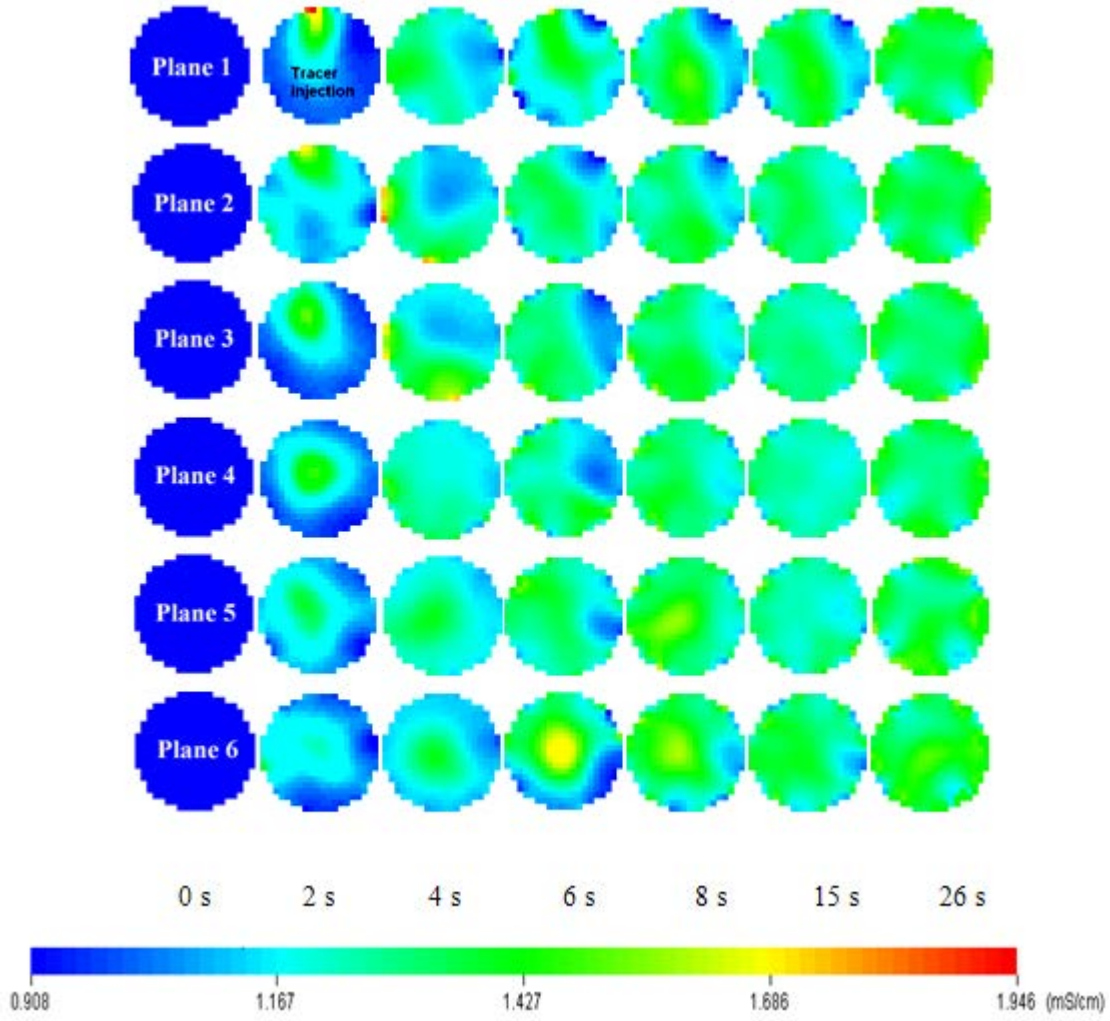

Fig. 5 2D tomograms recorded after the tracer injection in the batch mode (Maxblend impeller, 1% xanthan gum concentration, and N = 160 rpm).

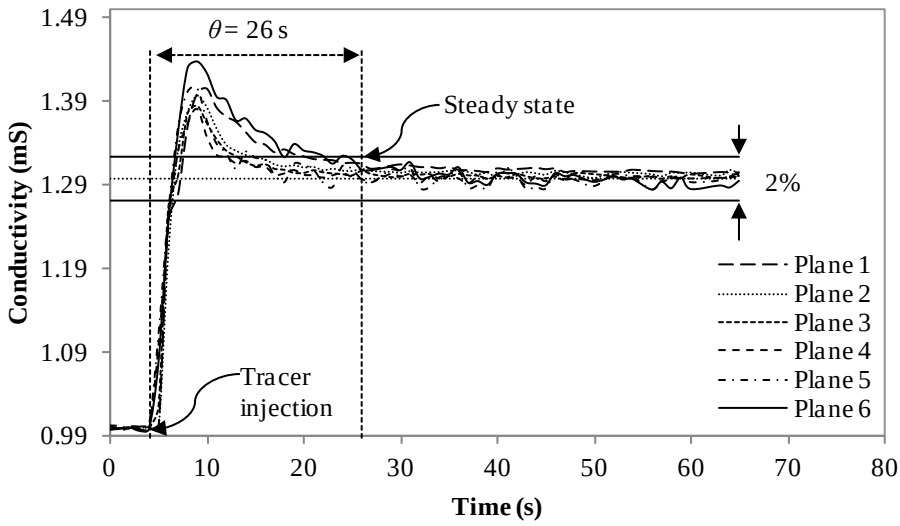

Fig. 6 Conductivity versus time for six tomography planes after the injection of the tracer in the batch mode (Maxblend impeller, 1% xanthan gum concentration, and N = 160 rpm).

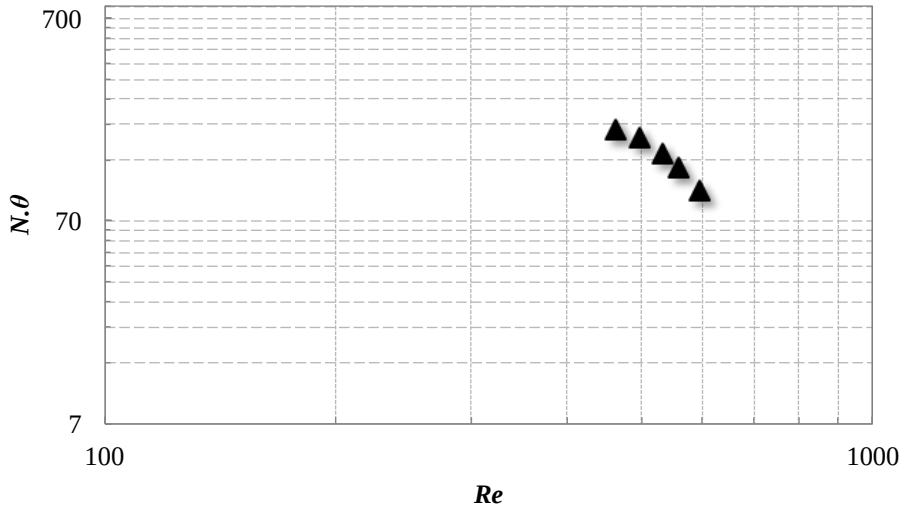

Fig. 7 Dimensionless mixing time as a function of Reynolds number for the scaba impeller.

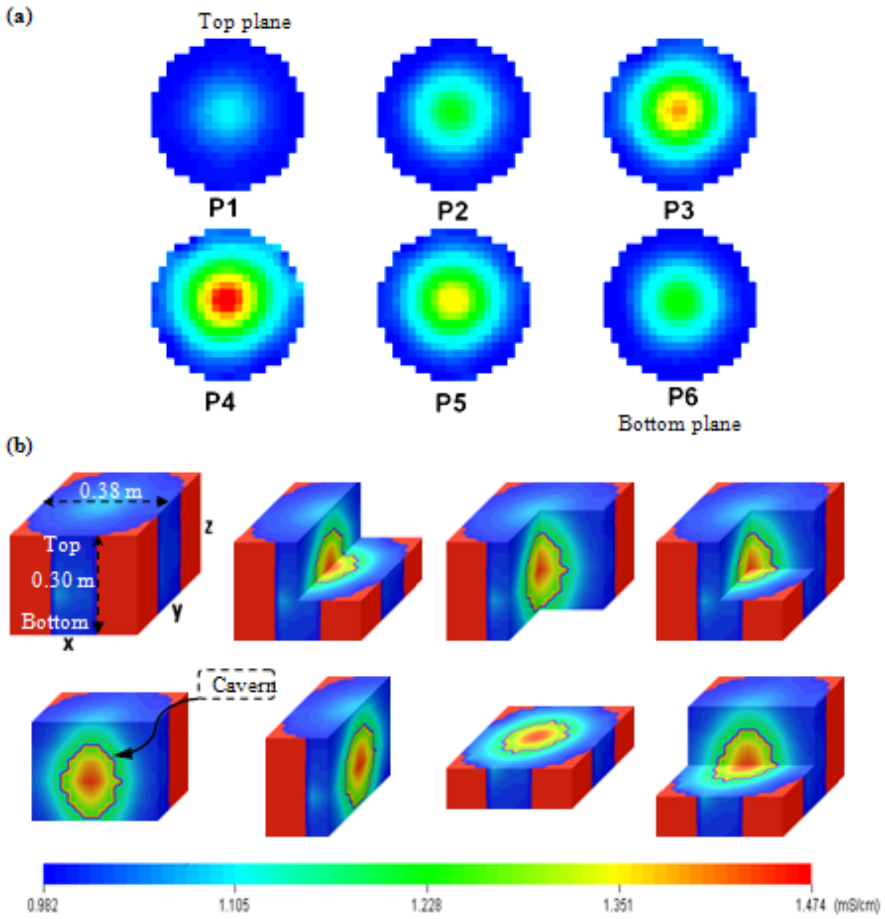

Fig. 8 3D images created from the 2D tomograms (0.5% xanthan gum solution, RT impeller, 21 rpm (*Re* = 8): (a) 2D tomogram and (b) 3D images generated using the Slicer Dicer software.

3.3 Cavern in a batch mode

In addition to the mixing time, the cavern size is also widely used to examine the mixing of the non-Newtonian fluids with yield stress in the batch mode. As mentioned earlier, the mixing of the pseudoplastic fluids possessing yield stress leads to the formation of a well-mixed turbulent zone around the impeller called the cavern. Fig. (8a) shows two dimensional (2D) tomograms of the cavern formation (0.5% xanthan gum solution,

RT impeller). The impeller was located on the plane *P*4. The tracer was injected on the impeller plane near the impeller hub using a syringe. The colors in these tomograms show the distribution of the tracer in the vessel. The blue color demonstrates the low-conductivity zones (i.e. the lower tracer concentrations). The red color represents the high-conductivity regions (i.e. the higher tracer concentration). The 2D tomogram shows that the tracer injected near the impeller hub remained within the cavern (well-mixed region) and no tracer was found in the surroundings, which is called stagnant zone. The spatial resolution of the ERT system was around 5% of the vessel diameter. This has been investigated through the phantom detection tests conducted by Holden et al. [55]. Fig. (8b) shows the 3D images generated from the 2D images using Slicer-Dicer software (PIXOTEC, USA). Based on the 3D images, the shape of the cavern was approximated by a right circular cylinder; therefore, the characteristics of the cavern can be described by the diameter and height of this region. The cavern diameter was measured on a horizontal plane cutting the impeller surface. The cavern height was measured on a vertical plane along the shaft and perpendicular to the horizontal plane of the impeller. To visualize how the tracer was dispersed in the opaque fluid (xanthan gum solutions), 3D images were generated by cutting the block in all possible ways on the *x*, *y* and *z*-axes to provide enough information about the cavern. Various 3D images shown in Fig. (8b) were generated by cutting the vertical plane at the center of the tank and/or the horizontal plane on the impeller surface.

Figs. (9a) and (9b) represent the dimensionless cavern diameter (D_c/D) as a function of power per unit volume and Reynolds number, respectively. The results show that as the impeller speed/power was increased, the cavern diameter (D_c) also increased for all concentrations. However, with respect to the xanthan gum concentration, the dimensionless cavern diameter (D_c/D) was observed as decreasing. This can be attributed to the effect of the yield stress, which increases with the xanthan gum concentrations. More stagnant regions are formed in the mixing vessel where shear stress fails to exceed yield stress, which reduces the cavern size. Therefore, the dimensionless cavern diameter decreased with an increase in the xanthan gum concentrations. ERT tests were repeated three times and the maximum standard deviation observed for the cavern diameter was about 0.95%.

Figs. (10a) and (10b) represents the cavern generated in the mixing of 1% xanthan gum solution with the RT impeller at N = 24 rpm (Re = 4, laminar regime) and N = 85 rpm (Re = 44, transitional regime), respectively. The results show that as the impeller speed (N) was increased from 24 to 85 rpm, the cavern volume also increased from 8 to 30% of the total volume of the fluid in the vessel. These figures indicate that the flow generated by the impeller at N = 24 and 85 rpm (in both laminar and transitional regimes) was not sufficient to disperse the injected tracer homogeneously throughout the vessel and thereby shows the presence of the dead volume. At a lower impeller speed the impeller imparted shear stress was not sufficient to overcome fluid yield stress; therefore, more stagnant regions were formed in the mixing vessel. Figs. (11a) and (11b) represents the effect of the fluid rheology on the cavern size generated in the mixing of 1% and 0.5% xanthan gum solutions, respectively (RT impeller, N = 24 rpm). The results show that as the xanthan gum concentration was decreased from 1.0 to 0.5%, the cavern volume increased from 8.0 to 12.5% of the total volume of the fluid in the vessel. This can be attributed to the effect of the yield stress, which reduces with a decrease in the xanthan gum concentration. As mentioned earlier, more stagnant regions are formed in the mixing vessel when the shear stress fails to exceed yield stress, which reduces the cavern volume. For the identical operating conditions (N = 24 rpm) when the xanthan gum concentration was decreased from 1.0 to 0.5%, the flow regime also changed from laminar (Re = 4) to transitional regime (Re = 12).

3.4 Deformation of cavern in a continuous-flow mode

ERT technique was also employed to investigate how the input-output flow in continuous-flow mixing affects the cavern formation. As described in the procedure, once the cavern remained unchanged in the batch mode, the feed and discharge pumps were turned on simultaneously. ERT data were collected and 2D tomography images were generated. Fig. (12) shows how the inlet and outlet flows deformed the cavern generated in the batch mode (RT impeller, N = 25 rpm**,** $Q = 1.60 \times 10^{-4}$ m^3 s^{-1}, and 1.0% xanthan gum). These images are presented in five columns in a time series (1st column from the left: Slicer Dicer *x*-axis image; 2nd column: Slicer Dicer *y*-axis image; 3rd column: Slicer Dicer block for the inverted position of the tank; 4th column: 2D tomograms from planes *P*1 to *P*6; and the 5th column: 3D images from planes *P*1 to *P*6 when the frames were stacked). In the 3rd column, the Slicer Dicer images of the tank are presented in an inverted position since it was difficult to view the bottom of the tank from the top. In this 3D image, the upper surface shows the bottom of the tank and the lower surface shows the top of the tank.

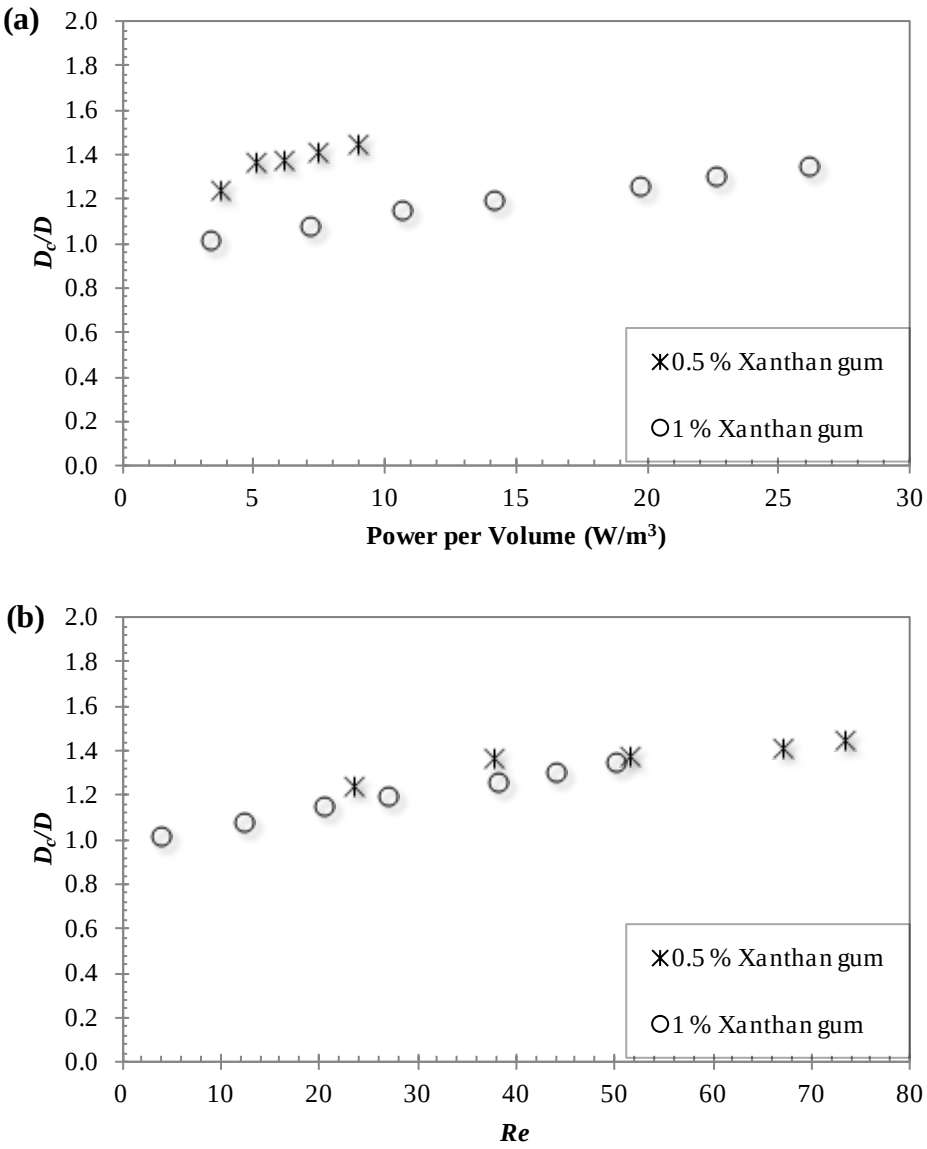

Fig. 9 Cavern generated in the mixing of xanthan gum solution (a) dimensionless cavern diameter (D_c/D) versus power per unit volume and (b) dimensionless cavern diameter (D_c/D) versus Reynolds number (Re).

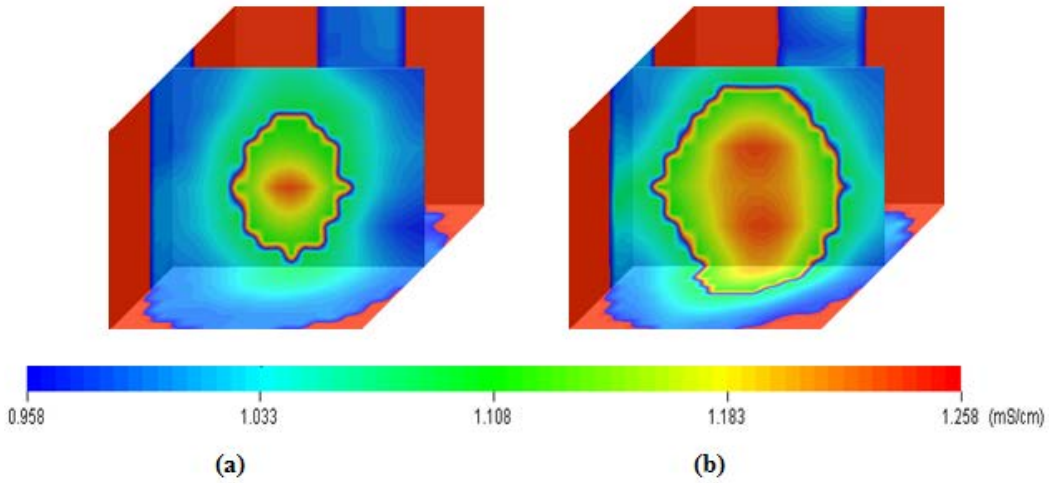

Fig. 10 Cavern generated in the mixing of 1% xanthan gum solution with the RT impeller at: (a) 24 rpm and (b) 85 rpm.

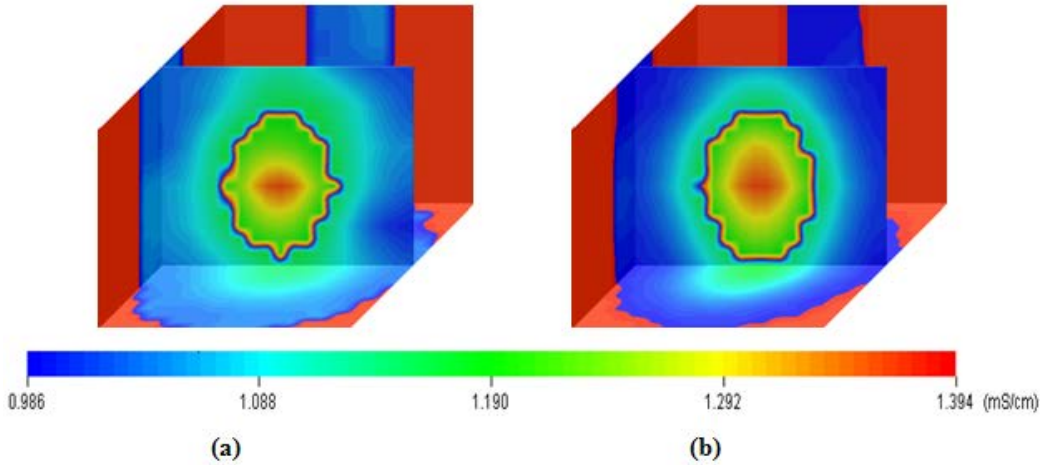

Fig. 11 Cavern generated with the RT impeller at N = 24 rpm in the mixing of: (a) 1% xanthan gum solution (b) 0.5% xanthan gum solution.

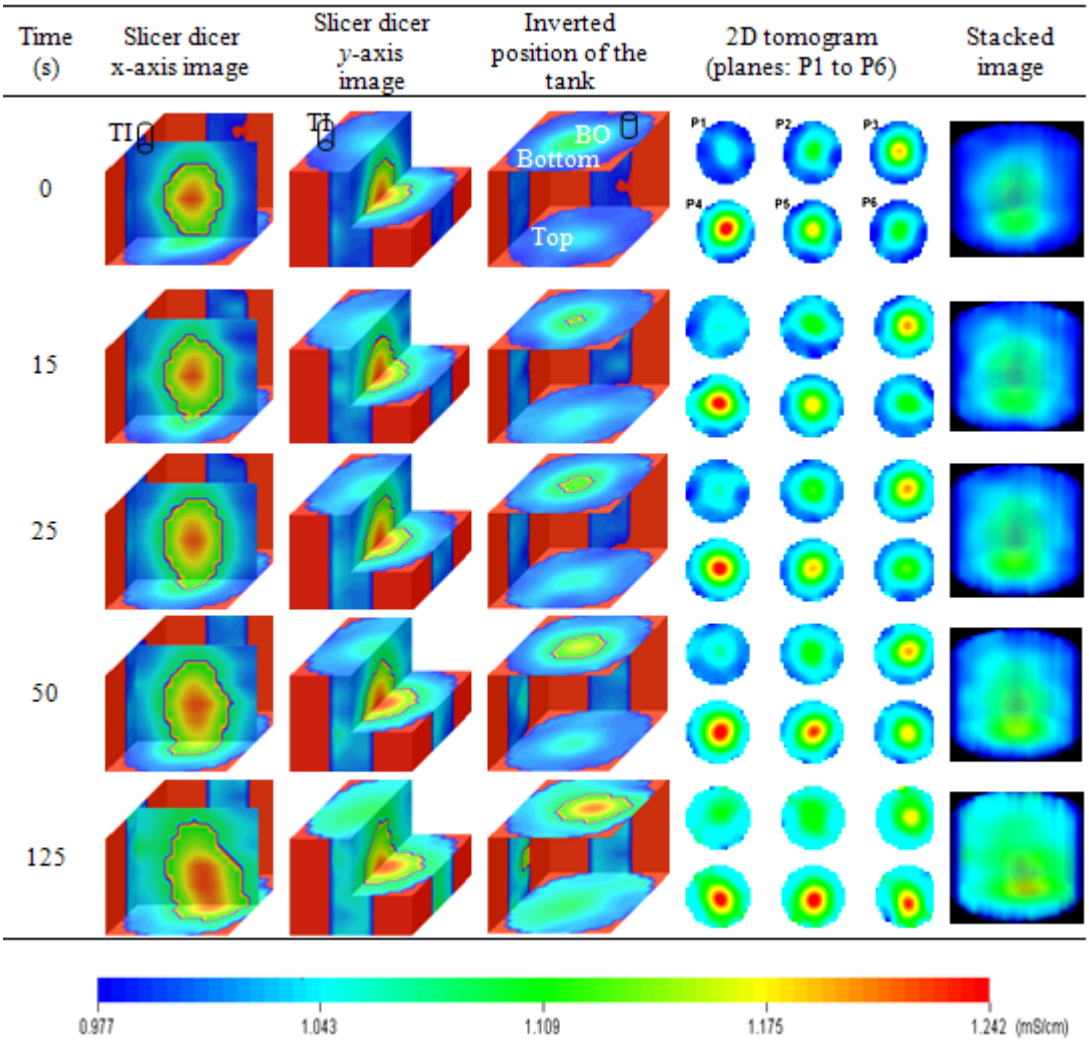

Fig. 12 Effect the inlet and outlet flow on the deformation of the cavern (RT impeller, N = 25 rpm, $Q = 1.60 \times 10^{-4}$ m^3 s^{-1}, and 1.0% xanthan gum).

The ERT images depicted in the first row of this figure were obtained at zero second (i.e. when the cavern size remained unchanged after the injection of the tracer in the batch mode and before the pumps were turned on). The images in the first row at zero second show that there was almost no tracer at the bottom plane

*P*6 in the 2D tomogram and the top surface of the inverted position of the tank. In Fig. (12), the images in the 2nd, 3rd, 4th, and 5th rows were taken at 15, 25, 50, and 125 s, respectively after the pumps were turned on in the continuous mode. The images in the second row clearly show that the cavern shape was slightly deformed at the bottom. This was due to the flow of fluid sucked from the bottom outlet (*BO*) by the discharge pump. At that moment, the tracer appeared at the top surface of the inverted position of the tank. As time passed, the fresh xanthan gum solution was continuously fed to the tank through the top inlet (*TI*) and the mixed solution was drawn from the vessel through the bottom outlet (*BO*). Due to this input-output flow, the cavern shape recorded in the batch mode was deformed in the continuous mode. The concentration of the tracer at the bottom plane *P*6 in the 2D tomogram and the top surface of the inverted position of the tank increased as shown in the subsequent images. It is clear from the images that the size of the cavern increased as the flow passed through the mixing tank. Finally, the volume of the deformed cavern increased approximately by 15.5% compared to the volume before the cavern deformation. This was due to the momentum added to the fluid in the mixing vessel by the input-output flow passing through it [56,57]. The extra momentum flux added to the fluid in the mixing vessel at the inlet position was about 99.92 kg m^{-1} s^{-2}.

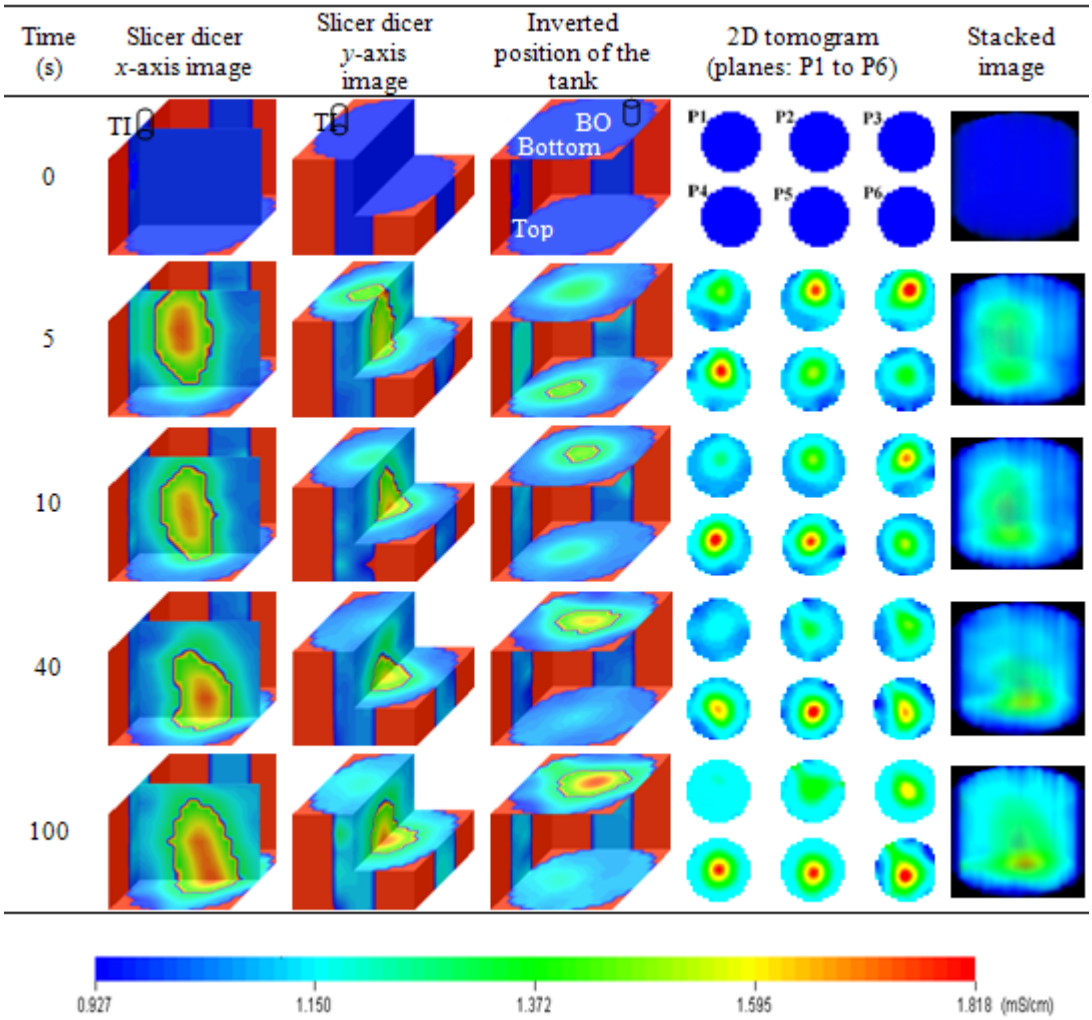

Fig. 13 Tracer distribution in the continuous-flow mixing system (Scaba impeller, N = 30 rpm, Q = 1.60 × 10^{-4} m^3 s^{-1}, and 1.0% xanthan gum).

3.5 Flow visualization in a continuous-flow mode

Further, the ERT technique was employed to visualize the tracer distribution in a continuous-flow mixing system. As mentioned in the procedure, the feed and discharge pumps were turned on simultaneously first and then the tracer was injected into the feed stream. ERT data were collected and 2D tomography images were reconstructed. The results are depicted in Fig. (13) to present how the tracer distributed in a continuous-flow

mixing system (Scaba impeller, N = 30 rpm**,** $Q = 1.60 \times 10^{-4}$ m^3 s^{-1}, and 1.0% xanthan gum). The blue color in the tomograms in the first row of Fig. (13) shows that only xanthan gum solution was present and there was no tracer in the tank at that moment (i.e. before the injection of the tracer). The images in the 2nd, 3rd, 4th, and 5th rows were taken at 5, 10, 40, and 100 s, respectively, after the injection of the tracer into the feed stream. In the second row, the color change in the ERT images shows that the tracer was injected into the feed at the top of the vessel. As the time passed, the fresh xanthan gum solution was added through the top inlet and the mixed solution was withdrawn from the vessel through the bottom outlet. The continuous flow of the fresh feed at the top of the tank pushed the tracer downwards while the mixed solution was sucked through the bottom outlet; therefore, in the 3rd row the tracer disappeared at plane *P1* in the 2D tomogram and the top surface of the tank in the Slicer Dicer images. Due to the nature of the yield-pseudoplastic fluid, the tracer was not observed in the dead zones, where the impeller imparted stresses were below the fluid yield stress. In fact, the formation of the cavern around the impeller can be seen in the subsequent images. Other than the impeller, the extra momentum generated by the inlet-outlet flow also facilitated the dispersion of the tracer inside the mixing tank and consequently the tracer channeled through the bottom outlet [58]. The extra momentum flux added to the fluid in the mixing vessel at the inlet position was about 99.92 kg m^{-1} s^{-2}.

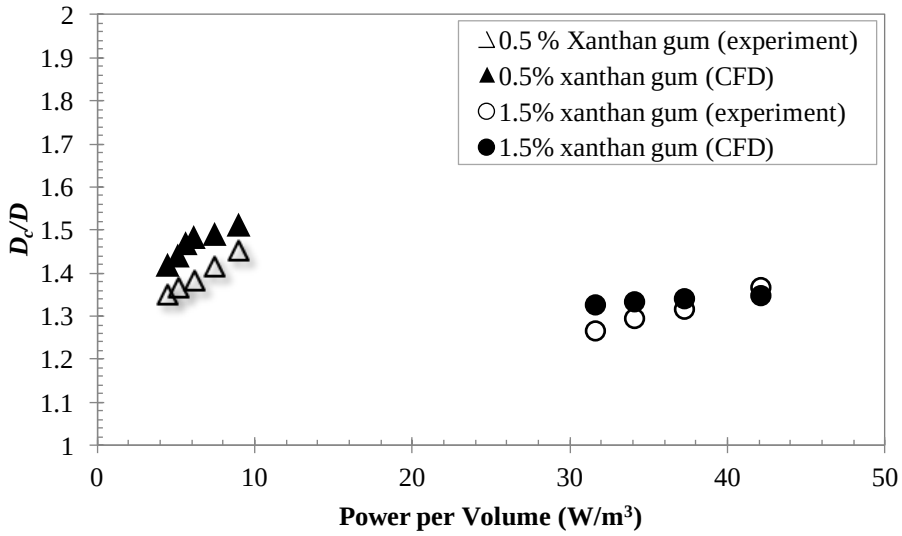

Fig. 14 CFD Model validation: Comparison between CFD and experimental data for cavern diameters (RT impeller, 0.5 and 1.5% xanthan gum solutions).

3.6 CFD Model Validation

Tomography results can be used to validate the CFD model developed for the mixing systems. To simulate the 3-D flow field generated by the RT impeller in the mixing of xanthan gum solution, the commercial CFD package ANSYS Fluent (version 14.5) was used in this study. The multiple reference frame (MRF) technique was employed to model the rotation of the impeller in the mixing tank [59]. The Herschel–Bulkley model was employed to describe the rheological behavior of xanthan gum solution (Yield-pseudoplastic fluid). Once the geometry was created, the number of cells used for discretization was determined by conducting a grid independence study. The optimal mesh of the model, which consisted of 817,077 cells, was used in all simulations. Boundary conditions applied on the geometry included (i) nonslip at the vessel wall and baffles ($v = 0$), (ii) zero normal velocity ($v_n = 0$) at the free surface, (iii) an inflow boundary condition for the vessel inlet, defining the inlet velocity from the volumetric flow rate of the feed, i.e, $v = 4Q/\pi d_i^2$ (where Q is the volumetric flow rate and d_i is the pipe inlet diameter), and (iv) an outflow boundary condition for the vessel outlet, implying zero normal diffusive flux for all flow variables ($\partial\varphi / \partial n = 0$) [60]. The discretized equations were solved using a segregated implicit scheme. CFD simulations were carried out using the followings schemes: (i) second order for pressure interpolation [60], (ii) power law for momentum interpolation [61], (iii) first order for temporal discretization [60], and (iv) SIMPLEC for pressure-velocity coupling [62]. The convergence history was monitored for the mass and x, y, and z velocities. Simulations were considered converged when the scaled residuals for each transport equation were below 10^{-7}. Most simulations required

more than 6000 iterations for convergence. The simulations were carried out using the supercomputing facilities of HPCVL (High Performance Computing Virtual Laboratory).

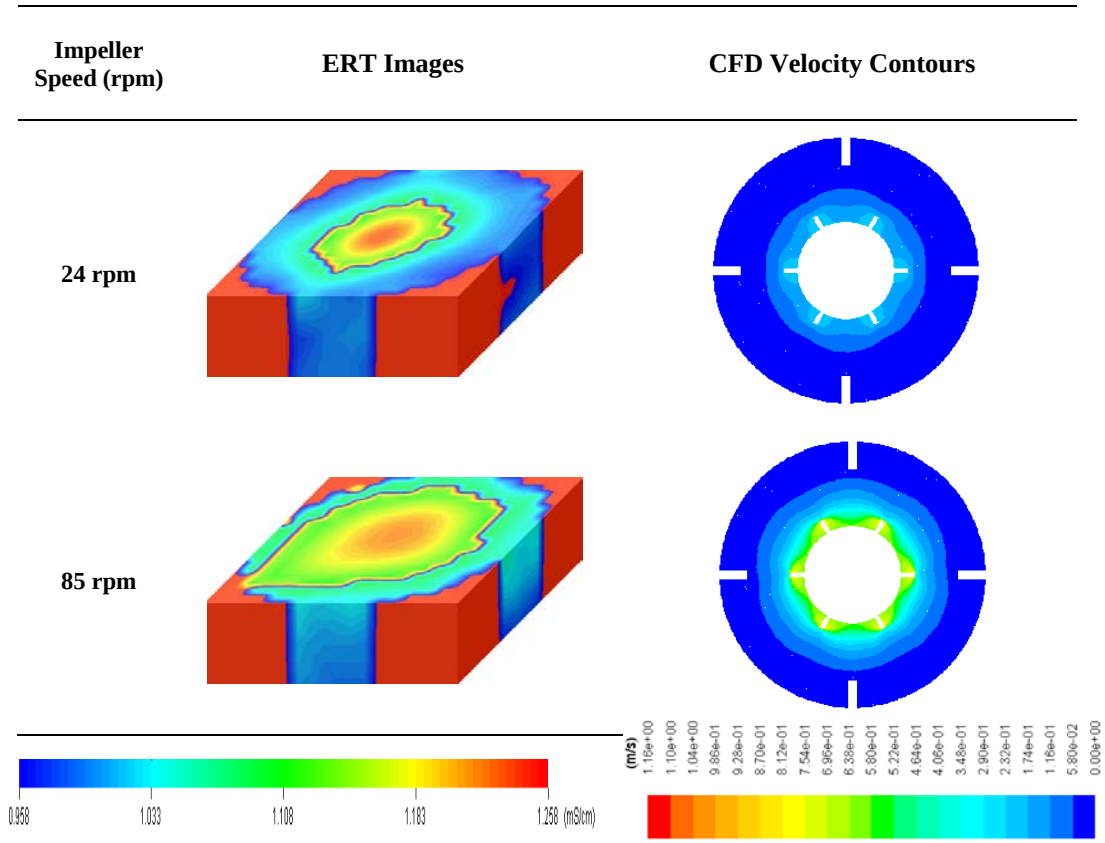

Fig. 15 Comparison of ERT tomogram with CFD velocity magnitude contour in the agitation of 1% xanthan gum solution using the RT impeller.

The results predicted by CFD simulations are reasonably accepted only if CFD model is validated through empirical or observed data. Therefore, it is very important to have some reliable experimental data in order to validate the CFD model. ERT can provide consistent qualitative and quantitative data upon which CFD model can be validated very realistically. Fig. (14) demonstrates the validation of the CFD model by comparing the cavern volume calculated using CFD with the cavern volume measured using ERT technique. The CFD and ERT results show good agreement with each other. These data show that as the impeller power per unit volume was increased, the cavern diameter also increased for all concentrations. Though, with respect to the xanthan gum concentration, the cavern diameter was observed as decreasing. This can be attributed to the effect of the yield stress, which increases with the xanthan gum concentrations. More stagnant regions are formed in the mixing vessel where shear stress fails to exceed yield stress, which reduces the cavern volume. Hence, the dimensionless cavern volume decreased with an increase in the xanthan gum concentrations. Fig. (15) also demonstrates the formation of cavern around the impeller in the mixing of 1% xanthan gum solution at 24 and 85 rpm visualized using tomography images and CFD model. The ERT and CFD results showed that as the impeller speed was increased from 24 to 85 rpm, the size of the cavern also increased. Hence, the experimental results obtained through ERT technique are very useful for validating the CFD model.

4 Conclusions

Electrical resistance tomography (ERT) was employed for studying the batch and continuous-flow mixing of non-Newtonian fluids possessing yield stress in a baffled mixing tank. Tomography data were utilized to measure the mixing time in the batch mode for the Maxblend impeller, to determine the cavern size in the batch mode for the RT impeller, to analyze the cavern deformation in the continuous mode for the RT impeller, and to visualize the flow pattern generated by the Scaba impeller inside the agitated tank in the continuous mode. Tomography images enabled us to identify the existence of non-ideal flows in the mixing of the non-

Newtonian opaque fluids inside the agitated vessels. ERT results show that as the impeller rotational speed was increased, the mixing time decreased. When the xanthan gum concentration was increased, the mixing time also increased. The results also show that as the impeller speed/power was increased, the cavern diameter (D_c) also increased for all concentrations. However, with respect to the xanthan gum concentration, the dimensionless cavern diameter (D_c/D) was observed as decreasing. This can be attributed to the effect of the yield stress, which increases with the xanthan gum concentrations. The cavern generated in a batch mode was deformed by the inlet-outlet flow in a continuous mode and the volume of the deformed cavern increased approximately by 15.5% compared to the volume before the cavern deformation. Finally, the tomography results for the cavern formation were successfully utilized to validate the CFD model.

Notation

A	area of interest in ERT measurement (m^2)
$C_{m,n,x,y}$	sensitivity coefficient (-)
D	impeller diameter (m)
d_i	pipe inlet diameter (m)
H	fluid height in the vessel (m)
K	consistency index (Pa s^n)
K_s	Metzner-Otto constant (-)
M	torque (N m)
n	power-law index (-)
n_e	number of electrodes (-)
N	impeller rotational speed (s^{-1})
P	power (W)
P_o	power number (-)
$P1$-$P6$	plane number (-)
Q	volumetric feed flow rate ($m^3\ s^{-1}$)
R	resistance (Ω)
Re	Reynolds number (-)
r, Φ, z	cylindrical coordinates (m, °, m)
T	tank diameter (m)
V	voltage (V)
ν	fluid velocity ($m\ s^{-1}$)
ν_n	normal velocity ($m\ s^{-1}$)

Greek Letters

$\dot{\gamma}$	shear rate (s^{-1})
$\dot{\gamma}_{avg}$	average shear rate (s^{-1})
η	apparent viscosity (Pa s)
θ	mixing time (s)
ρ	fluid density ($kg\ m^{-3}$)
τ_s	shear stress (Pa)
τ_y	fluid yield stress (Pa)

Abbreviations

2D	two-dimensions
3D	three-dimensions
BO	bottom outlet
CFD	computational fluid dynamics
DAS	data acquisition system
ERT	electrical resistance tomography
LDV	laser Doppler velocimetry
MRF	multiple reference frames

rpm	revolution per minute
RTD	residence time distribution
TI	top inlet

Acknowledgements

The financial support of the Natural Science and Engineering Research Council of Canada (NSERC, PGS D2), Ontario Graduate Scholarship (OGS) and Ontario Graduate Scholarship in Science and Technology (OGSST) are gratefully acknowledged.

References

[1] Paul E L, Atiemo-Obeng V A, Kresta S M (2004) Handbook of industrial mixing: Science and Practice, John Wiley & Sons, Inc., Hoboken, New Jersey.
[2] Zlokarnik M (2001) Stirring-theory and practice, Wiley-VCH, Weinheim.
[3] Masiuk S, Lacki H (1993) Power consumption and mixing time for Newtonian and non-Newtonian liquids mixing in a ribbon mixer. *Chemical Engineering Journal*, vol. 52, pp. 13–17.
[4] Raghav Rao K S M S, Joshi J B (1988) Liquid phase mixing in mechanically agitated vessels. *Chemical Engineering Communications*, vol. 74 (1), pp. 1–25.
[5] Cabaret F, Bonnot S, Fradette L, Tanguy P A (2007) Mixing time analysis using colorimentric methods and image processing. *Industrial & Engineering Chemistry Research*, vol. 42, pp. 5032–5042.
[6] Shervin C R, Raughley D A, Romaszewski R A (1991) Flow visualization scaleup studies for the mixing of viscoelastic fluids. *Chemical Engineering Science*, vol. 46, pp. 2867–2873.
[7] Lee K C, Yianneskis M (1997) Measurement of temperature and mixing time in stirred vessels with liquid crystal thermography. In: Proceedings of 9th European Conference on Mixing, (Ed(s).: Bertrand, J.; Villermaux, J.), Groupe Français de Génie des Procédés, Nancy, France, pp. 121–128.
[8] Distelhoff M F W, Marquis A J, Nouri J M, Whitelaw J H (1997) Scalar mixing measurements in batch operated stirred tanks. *Canadian Journal of Chemical Engineering*, vol. 75, pp. 641–652.
[9] Nere N K, Patwardhan A W, Joshi J B (2003) Liquid phase mixing in stirred. *Industrial & Engineering Chemistry Research*, vol. 42 (12), pp. 2661–2698.
[10] Rielly C D, Britter R E (1985) Mixing times for passive tracers in stirred tanks. In: Proceedings of 5th European Conference on Mixing, Wurzburg, West Germany; (Ed(s).: Stanbury, J.), BHRA Fluid Engineering, Cranfield, Bedford, pp. 365–375.
[11] Elson T P, Cheesman D J (1986) X-ray studies of cavern sizes and mixing performance with fluids possessing a yield stress. *Chemical Engineering Science*, vol. 41(10), pp. 2555–2562.
[12] Nienow A W, Elson T P (1988) Aspects of mixing in rheologically complex fluids. *Chemical Engineering Research and Design*, vol. 66, pp. 5–15.
[13] Hirata Y, Aoshima Y. (1996) Formation and growth of cavern in yield stress fluids agitated under baffled and non-Newtonian conditions. *Chemical Engineering Research and Design*, vol. 74(4), pp. 438–444.
[14] Arratia P E, Kukura J, Lacombe J, Muzzio F J (2006) Mixing of shear thinning fluids with yield stress in stirred tanks. *AIChE Journal*, vol. 52 (7), pp. 2310–2322.
[15] Galindo E, Nienow A W (1992) Mixing of highly viscous simulated xanthan fermentation broths with the Lightnin A-315 impeller. *Biotechnology Progress*, vol. 8(3), pp. 223–239.
[16] Solomon J, Elson T P, Nienow A W (1981) Cavern sizes in agitated fluids with a yield stress. *Chemical Engineering Communications*, vol. 11, pp. 143–164.
[17] Ein-Mozaffari F, Dumont G A, Bennington C P J (2003) Performance and design of agitated pulp stock chests. *Appita Journal*, vol. 56(2), pp. 127–133.
[18] Patel D, Ein-Mozaffari F, Mehrvar M (2011) Dynamic performance of continuous-flow mixing of pseudoplastic fluids exhibiting yield stress in stirred reactors. *Industrial & Engineering Chemistry Research*, vol. 50(15), pp. 9377–9389.
[19] Patel D, Ein-Mozaffari F, Mehrvar M (2013) Characterization of the continuous-flow mixing of non-Newtonian fluids using the ratio of residence time to batch mixing time. *Chemical Engineering Research and Design*, vol. 91 (7), pp. 1223-1234.

[20] Ein-Mozaffari F, Bennington C P J, Dumont G A (2007) Optimization of rectangular pulp stock mixing chest dimensions using dynamic tests, *Tappi Journal*, vol. 6(2), pp. 24–30.
[21] Patel D, Ein-Mozaffari F, Mehrvar M (2012) Improving the dynamic performance of continuous-flow mixing of pseudoplastic fluids possessing yield stress using Maxblend impeller. *Chemical Engineering Research and Design*, vol. 90(4), pp. 514–523.
[22] Saeed S, Ein-Mozaffari F, Upreti S R (2008) Using computational fluid dynamics to study the dynamic behavior of the continuous mixing of Herschel-Bulkley Fluids. *Industrial & Engineering Chemistry Research*, vol. 47, pp. 7465–7475.
[23] Patel D, Ein-Mozaffari F, Mehrvar M (2012) Effect of impeller type on continuous-flow mixing of non-Newtonian fluids in stirred vessels through dynamic tests. *Canadian Journal of Chemical Engineering*, vol. 90(2), pp. 290–298.
[24] Saeed S, Ein-Mozaffari F (2008) Using dynamic tests to study the continuous mixing of xanthan gum solutions. *Journal of Chemical Technology and Biotechnology*, vol. 83, pp. 559–568.
[25] Ford C, Ein-Mozaffari F, Bennington C P J, Taghipour F (2006) Simulation of mixing dynamics in agitated pulp stock chests using CFD. *AIChE Journal*, vol. 52(10), pp. 3562–3569.
[26] Aubin J, Kresta S M, Bertrand J, Xuereb C, Fletcher D F (2006) Alternate operating methods for improving the performance of continuous stirred tank reactors. *Chemical Engineering Research and Design*, vol. 84(A7), pp. 569–582.
[27] Khopkar A R, Mavros P, Ranade V V, Bertrand J (2004) Simulation of flow generated by an axial flow impeller - batch and continuous operation. *Chemical Engineering Research and Design*, vol. 82(A6), pp. 737–751.
[28] Samaras K, Mavros P, Zamboulis D (2006) Effect of continuous stream and agitator type on CFSTR mixing state. *Industrial & Engineering Chemistry Research*, vol. 45, pp. 4805–4815.
[29] Mavros P, Naude I, Xuereb C, Bertrand J (1997) Laser Doppler velocimetry in agitated vessels: Effect of continuous liquid stream on flow patterns. *Chemical Engineering Research and Design*, vol. 75(A), pp. 763–776.
[30] Roussinova V, Kresta S M (2008) Comparison of continuous blend time and residence time distribution models for a stirred tank. *Industrial & Engineering Chemistry Research*, vol. 47(10), pp. 3532–3539.
[31] Herschel W E, Bulkley R (1926) Measurements of consistency as applied to rubber-benzene solutions. In: Proceedings-American Society for Testing Materials, vol. 26(2), pp. 621–633.
[32] Vlaev D, Wang M, Dyakowski T, Mann R, Grieve B D (2000) Detecting filter cake pathologies in solid-liquid filtration: Semi-tech scale demonstration using electrical resistance tomography (ERT). *Chemical Engineering Journal*, vol. 77, pp. 87–92.
[33] Hosseini S, Patel D, Ein-Mozaffari F, Mehrvar M (2010) Study of solid-liquid mixing in agitated tanks through electrical resistance tomography. *Chemical Engineering Science*, vol. 65 (4), pp. 1374–1384.
[34] Hosseini S, Patel D, Ein-Mozaffari F, Mehrvar M (2010) Study of solid-liquid mixing in agitated tanks through computational fluid dynamics modeling. *Industrial & Engineering Chemistry Research*, vol. 49 (9), pp. 4426–4435.
[35] Tahvildarian P, Ng H, D'Amato M, Drappel S, Ein-Mozaffari F, Upreti S (2011) Using electrical resistance tomography images to characterize the mixing of micron-sized polymeric particles in a slurry reactor. *Chemical Engineering Journal*, vol. 172, pp. 517–525.
[36] Patel D, Ein-Mozaffari F, Mehrvar M (2013) Using tomography to characterize the mixing of non-Newtonian fluids with a Maxblend impeller. *Chemical Engineering & Technology*, vol. 36 (4), pp. 687–695.
[37] Pakzad L, Ein-Mozaffari F, Chan P (2008) Using electrical resistance tomography and computational fluid dynamics modeling to study the formation of cavern in the mixing of pseudoplastic fluids possessing yield stress. *Chemical Engineering Science*, vol. 63(9), pp. 2508–2522.
[38] Hamood-ur-Rehman M, Dahman Y, Ein-Mozaffari F (2012) Investigation of mixing characteristics in a packed-bed external loop airlift bioreactor using tomography images. *Chemical Engineering Journal*, vol. 213, pp. 50–61.
[39] Gumery F, Ein-Mozaffari F, Dahman Y (2011) Macromixing hydrodynamic study in draft-tube airlift reactors using electrical resistance tomography. *Bioprocess and Biosystems Engineering*, vol. 34 (2), pp. 135–144.

[40] Zhao Z F, Mehrvar M, Ein-Mozaffari F (2008) Mixing time in an agitated multi-lamp cylindrical photoreactor using electrical resistance tomography. *Journal of Chemical Technology and Biotechnology*, vol. 83(12), pp. 1676–1688.
[41] Seagar A D, Barber D C, Brown B H (1987) Theoretical limits to sensitivity and resolution in impedance imaging. *Clinical Physics and Physiological Measurement*, vol. 8, pp. 13–31.
[42] Tapp H S, Williams R A (2000) Status and applications of microelectrical resistance tomography. *Chemical Engineering Science*, vol. 77, pp. 119–125.
[43] Dickin F, Wang M (1996) Electrical resistance tomography for process applications. *Measurement Science* and *Technology*, vol. 7(3), pp. 247–260.
[44] Mann R, Wang M, Dickin F J, Dyakowski T, Holden P J, Forrest A E, Edwards R B (1996) Resistance tomography imaging of stirred vessel mixing at plant scale. *Institution of Chemical Engineering Symposium Series*, vol. 140, pp. 155–166.
[45] Williams R A, Beck M S (1995) Process tomography: principles, techniques and applications, Butterworth-Heinemann.
[46] Mann R, Williams R, Dyakowski T, Dickin F, Edwards R (1997) Development of mixing models using electrical resistance tomography. *Chemical Engineering Science*, vol. 52(13), pp. 2073–2085.
[47] Gisser D G, Issacson D, Newell J (1987) Current topics in impedance imaging. *Clinical Physics and Physiological Measurement*, vol. 8 (A), pp. 36–46.
[48] Madupu A, Mazumdar A, Jinsong Z, Roelant D, Srivastava R (2005) Electrical resistance tomography for real-time mapping of the solid-liquid interface in tanks containing optically opaque fluids. In: Proc. SPIE - The International Society for Optical Engineering, 5674, pp. 36–46.
[49] Wang M (2002) Inverse solutions for electrical impedance tomography based on conjugate gradients methods. *Measurement Science and Technology*, vol. 13, pp. 101–117.
[50] Kotre C J (1989) A sensitivity coefficient method for the reconstruction of electrical impedance tomograms. *Clinical Physics and Physiological Measurement*, vol. 10 (3), pp. 275–281.
[51] Metzner A B, Otto R E (1957) Agitation of non-Newtonian fluids. *AIChE Journal*, vol. 3(1), pp. 3–11.
[52] Devals C, Heniche M, Takenaka K, Tanguy P A (2008) CFD analysis of several design parameters affecting the performance of the Maxblend impeller. *Computers and Chemical Engineering*, vol. 32, pp. 1831–1841.
[53] Fradette L, Thome G, Tanguy P A, Takenaka K (2007) Power and mixing time study involving a Maxblend impeller with viscous Newtonian and non-Newtonian fluids. *Chemical Engineering Research and Design*, vol. 85 (A11), pp. 1514–1523.
[54] Iranshahi A, Devals C, Heniche M, Fradette L, Tanguy P A, Takenaka K (2007) Hydrodynamics characterization of the Maxblend impeller. *Chemical Engineering Science*, vol. 62, pp. 3641–3653.
[55] Holden P J, Wang M, Mann R, Dickin F J, Edward R B (1998) Imaging stirred-vessel macromixing using electrical resistance tomography. *AIChE Journal*, vol. 44 (4), pp. 780–790.
[56] Patel D, Ein-Mozaffari F, Mehrvar M (2013) Using tomography technique to characterize the continuous-flow mixing of non-Newtonian fluids in stirred vessels. *Chemical Engineering Transactions*, 32, 1465-1470.
[57] Patel D, Ein-Mozaffari F, Mehrvar M (2014) Tomography images to analyze the deformation of the cavern in the continuous-flow mixing of non-Newtonian fluids. *AIChE Journal*, 60 (1), 315-331.
[58] Patel D, Ein-Mozaffari F, Mehrvar M (2014) Using tomography to visualize the continuous-flow mixing of biopolymer solutions inside a stirred tank reactor. *Chemical Engineering Journal*, 239, 257-273.
[59] Luo J Y, Gosman A D, Issa R I (1994) Prediction of impeller-induced flows in mixing vessels using multiple frames of reference. *Institution of Chemical Engineering Symposium Series*, vol. 136, pp. 549–556.
[60] Versteeg H K, Malalasekera W (2007) An introduction to computational fluid mechanics-the finite volume method, 2nd ed.; Pearson Prentice Hall: Upper Saddle River, NJ.
[61] Patankar S V (1980) Numerical heat transfer and fluid flow; Hemisphere Publishing Corp., Taylor & Francis Group: New York.
[62] Van Doormal J P, Raithby G D (1984) Enhancements of the SIMPLE method for predicting incompressible fluid flows. *Numerical Heat Transfer*, vol. 7, pp. 147–163.